Measurement and Statistical Analysis of Co-60 Decay Using Scintillation Detectors

Syed Murtaza Husain
PHY 353L Modern Laboratory
Department of Physics
The University of Texas at Austin
Austin, TX 78712, USA

October 16, 2025

Abstract

Through the use of a scintillation radiation detector and a signal processing setup involving single and multi-channel analyzers, we measured the radioactive decay of ^{60}Co. We recorded γ-emissions at the characteristic 1.17 MeV and 1.33 MeV lines and compared their decay rates, finding a significant difference of $R_{1.17}/R_{1.33} = 1.3050 \pm 0.0011$, which is consistent with theoretical detector efficiency. Statistical analysis verified that the counting process follows Poisson behavior. The normal approximation was valid for mean counts above $\mu \approx 20$, while noticeable deviations appeared below this threshold, where the distribution had Poisson characteristics. The standard deviation scaled with the square root of the mean, $\sigma \propto \sqrt{\mu}$, when Poisson statistics dominate, confirming the expected Poisson variance relationship. We carried out a noise and temporal analysis in addition to standard analysis: Interarrival-time analysis confirmed exponential waiting times consistent with a memoryless process (KS $p = 0.52$), and Allan variance testing revealed $\sigma_y(\tau) \propto \tau^{-1/2}$ scaling at short times, with a slight flattening at longer τ indicating slow drift in the counting rate.

1 Introduction

1.1 Physics Motivation

Radioactive decay is the process that a nucelus of an atom undergoes when it is an unstable isotope, and is a fundamental part of nuclear physics. It was discovered in 1896 by Antoine Becquerel, when observing uranium salts emitting rays that can darken photographic plates [8]. This radiation was found to be unaffected by temperature or pressure changes, and was very energetic.

In 1903, Marie Curie discovered that uranium electrified the air around radioactive samples, and later discovered that other elements were radioactive, such as Thorium, along with discovering the elements Polonium and Radium [5].

The properties of radioactive decay, since its discovery, has since been harnessed to create items used in our daily lives, such as smoke detectors. Other applications include radiometric dating, medical imaging, and cancer treatment, as well as nucelar reactors which produce energy through the fission of radioactive isotopes.

Decay processes are random in nature, with emissions happening at rates that are varied when observed over short periods. However, these processes can be statistically analyzed to understand their characteristics. Understanding radioactive decay is important for its usefulness and the potential for future innovations that can be developed from it.

1.2 Theoretical Background

Radioactive decay is a random process that occurs at the atomic level. An unstable nucleus loses energy by emitting radiation, including alpha decay (emission of a helium nucleus), beta decay (emission of an electron or positron), and gamma decay (emission of high-energy photons). The probability of decay is found using by the

decay constant λ, which is related to the half-life $T_{1/2}$ of the isotope. The number of undecayed nuclei $N(t)$ at time t is given by:

$$N(t) = N_0 e^{-\lambda t}$$

where N_0 is the initial number of nuclei and λ is the decay constant. The half-life is given by

$$T_{1/2} = \frac{\ln 2}{\lambda}.$$

Because decay is a stochastic and discrete process, emission counts will follow the Poisson distribution, which has well known statistical attributes. The distribution can be given by the formula:

$$P(X = x) = \frac{\mu^x e^{-\mu}}{x!} \tag{1}$$

Where μ is the mean number of events over a time interval, and x is the number of events we want to calculate the probability for [7]. The standard deviation of the distribution grows with:

$$\sigma_N = \sqrt{N}$$

Which interestingly also means that the variance is equal to the mean for this type of distribution. This can also be used to understand error estimates in measured count rates.

In this experiment, we measure the decay of a Co-60 source, which undergoes beta decay to transform into a Ni-60 excited atom, which is stable but emites two gammay rays to reach its ground state. This process is shown below [6]:

$$^{60}Co \rightarrow \ ^{60}Ni^* + \beta^-$$
$$^{60}Ni^* \rightarrow \ ^{60}Ni + \gamma + \gamma$$

To drop from the excited state, the Ni atom will emite one gamma ray at 1.17 Mev, and then another one at 1.33 Mev to drop another level to reach its ground state. A visual representation of the decay scheme is shown in figure 1. These photon emissions can be detected using our equipment in this experiment.

In the limit of large N, the Poisson distribution exhibits behavior of an approximately normal distribution [7]. It is otherwise usually right-skewed. This is useful to know because it allows us to determine a very good estimate of

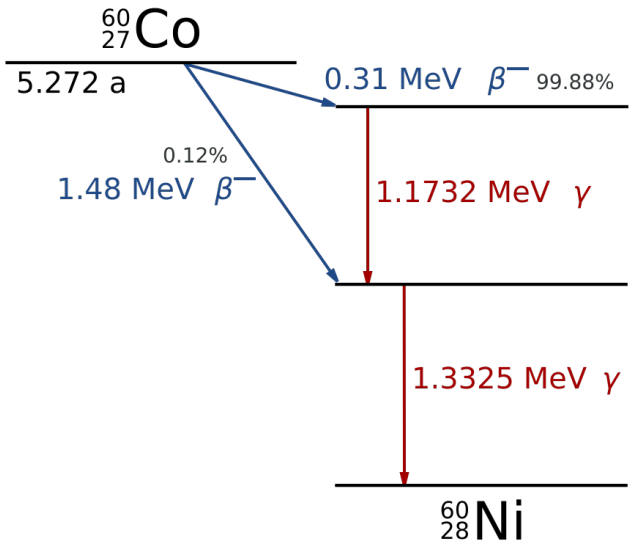

Figure 1: Decay scheme for Co-60 atom. Beta and Gamma emissions take place as the nucleus drops to a stable configuration and rids itself of excess energy in the form of γ rays. Image licensed under CC BY-SA 3.0, via Wikimedia Commons.

our measurement uncertainty after a sufficient detection period to achieve large N. A common limit for large N is $N > 10$, and we expect counts much higher than this for sufficiently long measurement periods. There are several statistical tools we utilize to examine the distributions and rates of decay processes: The Kolmogorov-Smirnov (D) statistic is used to compare two empirical distributions and is useful under finite sample conditions [2]. Using the scikit-learn implementation of the D statistic, we can test whether or not the rates of the two decay processes are equal. The chi-squared test measures the difference between our observed frequencies of data and the expected frequencies, or our null hypothesis. For binned data, it is defined as

$$\chi^2 = \sum_{i=1}^{N_{\text{bins}}} \frac{(O_i - E_i)^2}{E_i},$$

where O_i and E_i are the observed and expected counts in bin i. The χ^2 test gives us a normalized measure of deviation, but the log-likelihood metric tells us how probable the observed data are under a specific statistical model (again, our hypothesis). For a Poisson process like the one we observe, the likelihood of observing a set of counts

$\{O_i\}$ with expected means $\{\lambda_i\}$ is

$$\mathcal{L} = \prod_{i=1}^{N_{\text{bins}}} \frac{\lambda_i^{O_i} e^{-\lambda_i}}{O_i!}.$$

And this becomes the log-likelihood function:

$$\ln \mathcal{L} = \sum_{i=1}^{N_{\text{bins}}} \left(O_i \ln \lambda_i - \lambda_i - \ln O_i! \right).$$

A larger $\ln \mathcal{L}$ corresponds to a model that is more consistent with the observed data. Log-likelihoods are useful for comparing models, such as determining whether a Poisson or Gaussian distribution better describes a given dataset.

1.3 Noise Analysis Background

In time-domain stability analysis, Allan variance is a metrics that is used as a statistical measure of noise characteristics as well as long-term drift. Unlike classical variance, which diverges for certain noise types the Allan variance converges and gives us information about time varying drift [1].

For a time series of average count rates $\bar{y}_i$ computed over non-overlapping intervals of duration τ, the Allan variance is defined as

$$\sigma_y^2(\tau) = \frac{1}{2(N-1)} \sum_{i=1}^{N-1} \left(\bar{y}_{i+1} - \bar{y}_i \right)^2, \tag{2}$$

where N is the number of averaged samples. The Allan deviation, given by $\sigma_y(\tau) = \sqrt{\sigma_y^2(\tau)}$, shows the fractional instability of our measurement as a function of the averaging time τ.

For purely random noise, like our Poisson-distributed counting statistics, the Allan deviation is expected to scale with:

$$\sigma_y(\tau) \propto \tau^{-1/2}, \tag{3}$$

which means that averaging over longer times reduces noise by the square root of the integration time [13]. Deviations from this theoretical behavior could be due to correlated fluctuations or systematic drift components in the signal.

Another noise characteristic we can measure is interarrival time analysis, which examines the probability distribution of time intervals between successive detection events [9]. For a Poisson process with a constant mean rate λ, the interarrival times Δt are expected to follow an exponential probability density function:

$$p(\Delta t) = \lambda e^{-\lambda \Delta t},$$

where λ is the mean event rate.

1.4 Equipment Background

There are several key pieces of equipment that must be used to effectively measure radioactive decay in this experiment. Among them are our Ortec 905-3 scintillation radiation detectors (SRDs), pre-amplifiers and amplifiers, single-channel and multi-channel analyzers (SCAs, MCAs) and NI USB-6341 input module that allows us to interface with the labview software on the laboratory computer. When a gamma ray interacts with an SRD, a pules of light is produced via atoms going from excited back to their ground state. This pulse is converted into an electric pulse using photomultiplier tubes (PMTs), which contain photocathodes, electrodes, and dynodes to multiply the number of electrons being produced [10]. A diagram of an SRD can be seen in figure 2. One importat quality of SRDs is their differing response to γ rays of different energies. Higher energy energy photons, due to Compton scattering, sometimes are undetectable by the device. We explore the efficiency dropoff of our particular SRD in section 2.6, and analyze how our data is affected by this.

Another important component is the pre-amplifier, which has the purpose of strengthening the signal while minimizing noise as much as possible. After the pre-amplification stage, the signal is sent to an amplifier with coarse and fine gain controls for further strengthening. Next, the signal is sent to either an SCA or MCA, both of which convert this electrical signal to a digital one.
The distinction between SCAs and MCAs lies in the width of the pulse window that they can measure. An SCA has to be set at a specific window in which it can measure incoming energy, and it measures the number of detections, or counts, that occur within that range. Meanwhile, an MCA can detect across many windows and produces a spectrum of detections across the energies that its windows cover [4].

After we have our digital signal output into the MCA or USB hub, our lab computer can process the signal using one of two softwares. For MCA use, we utilize the MAESTRO software, which outputs ASCII .spe files that

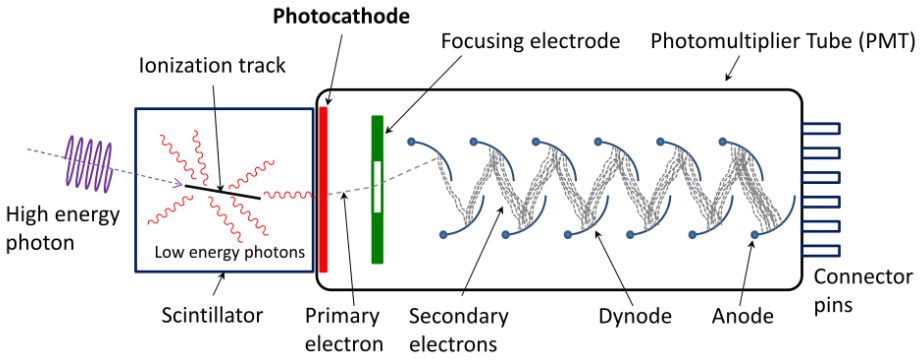

Figure 2: Schematic of a photomultiplier tube coupled to a scintillator. Gamma rays interact with the scintillator to produce photons which are converted to electrons and multiplied at the photocathode and PMT. Image licensed under CC BY-SA 3.0, via Wikimedia Commons.

give metadata as well as a bin vs counts reading that is accumulated over the live run time. Labview is used for SCA use, and returns a simple counts vs time plot for the energy band it is observing. Out experimental setup is shown in figure 3.

1.5 Our Approach

Using our SRD, we detect the gamma ray emission of a Co-60 sample and measure the stochastic properties of its decay. This signal will be sent through the pre-amplification and amplification stages and then finally converted into digital signals using an MCA. We will also use SCAs to measure finer bands of energy emissions and characterize the emissions across the spectrum of Co-60. Following this process, we will conduct rigorous statistical analysis to determine properties of the emsission distributions, including the average count values, standard deviation of the distributions, and other attributes.

2 Experimental Setup

2.1 Equipment Setup

To begin the experiment, we connected our Ortec 905-3 SRD to a pre-amplifier, amplifier, and MCA. Using BNC tees, we also observed the amplifier output on an oscilloscope. Following some trial and error, we determined that setting the pre-amplifier to 200 pF and the amplifier to 10 dB was sufficient to see emission peaks on the oscilloscope. After powering on the PMT with a 0.7 kV power supply and connecting our equipment to the MAESTRO software on the lab computer, we were able to see radiation counts being collected from the Co-60, that had the expected energy peaks and shape. We took several measurements of the spectrum for different amounts of time.

We also make a note that out of the several Ortec 490b amplifiers, only one was operational. We determined this by noticing that the count number for the PMT using the malfunctioning amplifier detected counts about 1/5 as large as the functioning one, as well as the number of counts not increasing with increased gain. Originally, we were planning to make use of both radiation detectors and take simultaneous spectra of the source, but we were unfortunately unable to do so.

2.2 Measurement Error Analysis

THere are several sources of error present in this experiment. The first of these is the presence of background noise in our PMT signal due to things like room light. To combat this, we take a bakground spectra and calculate a count rate for each MCA bin, $R_i = N_i/T_{live}$. This has an uncertainty $\sigma_R = \frac{\sqrt{N}}{T}$ since it follows a Poisson distribution. When subtracting the background spectra from the signal, we simply calculate the amount of counts to subtract from each bin using the count rates and live time. The error for the final signal propagtes as $\sigma_{Subtracted} = \sqrt{\sigma_{NS}^2 + \sigma_N^2}$ [3]. There is also some uncertainty in determining the peaks of the γ emissions using the MCA and SCAs.

For SCAs, the uncertainty has to do with the fluctuation in the counted number of events within a window. Following the standard deviation for a Poisson distribution, the uncertainty of SCA measurements is $\sigma_{N_{\mathrm{SCA}}} = \sqrt{N_{\mathrm{SCA}}}$.

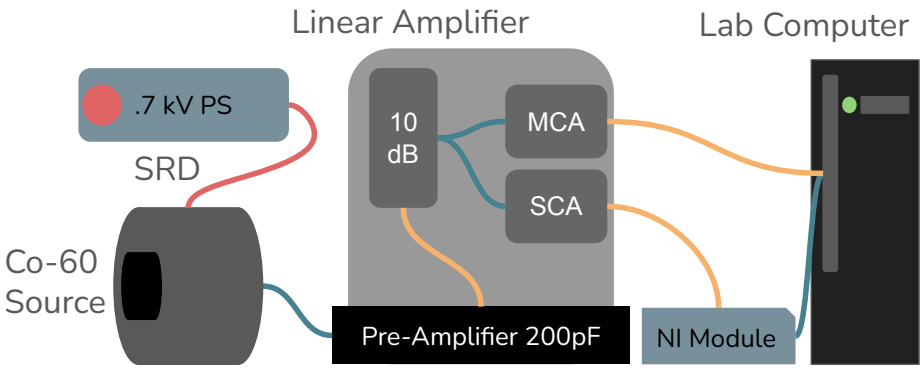

Figure 3: Schematic of our experimental setup. Signal processing chain consisted of a pre-amplifier taking in SRD detections of the Co-60 source and outputting the analog signal to either SCA or MCA modules, from which we obtained readings with either the NI or MAESTRO software.

For MCAs, the same reasoning applies, except each bin is now poisson distributed. Then in each channel, the uncertainty is $\sigma_{N(x_i)} = \sqrt{N(x_i)}$, and the total uncertainty depends on the number of events counted as well as the spread. As justified in section 1, we can treat a Poisson distribution with large N to be similar to a Gaussian distribution. Using this, we can approximate the total uncertainty as

$$\sigma_{x_{\text{peak}}} \approx \frac{\sigma_{\text{ch}}}{\sqrt{N_{\text{peak}}}}$$

2.3 Energy Calibration

Our measurements using the MCA can be calibrated from channel number to energy in MeV by following a simple peak-fit where we apply the two known Co-60 energies of $E_1 = 1173.23\ MeV, E_2 = 1332.49\ MeV$ to the two right peaks of the distribution, following the known spectra. Uncertainty in this fit is small and is mostly due to the MCA channel resolution of $\pm\frac{1}{2}$ channel [12].

This is essentially a linear fit:

$$E(x) = a + b\,x, \qquad b = \frac{E_2 - E_1}{x_2 - x_1}, \qquad a = E_1 - b\,x_1.$$

Uncertainties in x_1 and x_2 propagate in quadrature

$$\sigma_b = \frac{E_2 - E_1}{(x_2 - x_1)^2}\sqrt{\sigma_{x_1}^2 + \sigma_{x_2}^2},$$

$$\sigma_a = \sqrt{\sigma_{E_1}^2 + x_1^2\sigma_b^2 + b^2\sigma_{x_1}^2}.$$

The uncertainty in energy at any channel x is then

$$\sigma_E = \sqrt{\sigma_a^2 + x^2\sigma_b^2 + b^2\sigma_x^2}.$$

Given that we're assuming negligible σ_x, the error is dominated by uncertainty in x_1, x_2.

A similar approach can be applied to calibrating the SCA data, with the caveat that we must find the mapping from the SCA dial values to energy in MeV. We can do this by applying the two known ^{60}Co energies of $E_1 = 1173.23$ MeV and $E_2 = 1332.49$ MeV to the two photopeaks we observe in an SCA count-rate scan. The corresponding dial settings D_1 and D_2 were identified from the measured rate–threshold curve, following the known energy of the spectrum. The uncertainty in this fit is due b the dial precision and SCA response [12].

We can again use a linear model:

$$E(D) = A + B\,D, \qquad B = \frac{E_2 - E_1}{D_2 - D_1}, \qquad A = E_1 - B\,D_1.$$

Uncertainties in D_1 and D_2 add in quadrature:

$$\sigma_B = \frac{E_2 - E_1}{(D_2 - D_1)^2}\sqrt{\sigma_{D_1}^2 + \sigma_{D_2}^2},$$

$$\sigma_A = \sqrt{\sigma_{E_1}^2 + D_1^2\sigma_B^2 + B^2\sigma_{D_1}^2}.$$

The uncertainty in energy at any dial position D is

$$\sigma_E = \sqrt{\sigma_A^2 + D^2\sigma_B^2 + B^2\sigma_D^2}.$$

The total error is largely due to the uncertainty in locating the two reference peaks because we can assume that σ_D is relatively small.

Because we utilize a lower level SCA cutoff and an energy

window, the energies at the bounds are then:

$$E_L = A + B\,D_{\mathrm{LLD}}, \qquad E_U = A + B\,(D_{\mathrm{LLD}} + D_{\mathrm{Win}}),$$

with an energy window width of

$$\Delta E = B\,D_{\mathrm{Win}}.$$

2.4 SCA Data Collection

To obtain our SCA data, we first perform a sweep of the spectrum and record the fit parameters, before centering the lower SCA level on the 1.33 MeV peak. We decrease our bin size with the SCA width dial until it is at a dial reading of 1, which translates to an energy width of 0.023 ± 0.0038 MeV when using our fit and considering the least count of tenths on the dials. We take two measurements of this emission with different live times of 400 and 1200 seconds. Figure 4 shows raw measurements.

2.5 MCA Data Collection

For the MCA connection, we vary the runtime of the cllection process for future statistical analysis. We obtain the characteristic spectra of the sample, which is shown in 5. Five runs are taken, from 401s to 2000s, for later analysis of how the standard deviation shifts with mean observations and number of observed events. In addition to this, we take 20 1s short interval MCA measurements that will contain low counts, less than our limit for large N which determine whether or not the data will be relatively Poisson or Gaussian. This will allows us to observe more Poisson behavior that we expect to be exhibited over short time intervals.

2.6 Detector Droppoff Calibration

The detection efficiency $\varepsilon(E)$ of a NaI(Tl) SRD decreases with increasing photon energy because of the reduced photoelectric absorption probability and Compton scattering. This reduction affects our measured count rates for the two γ-ray peaks, even if both are emitted with equal intensity from the same isotope.

A decay process that produces two γ rays being detected by a constant efficiency detector should have:

$$R_1 = R_2 = \text{constant}.$$

But in practice, NaI(Tl) efficiency declines with energy [11] as:

$$\frac{R_1}{R_2} = \frac{\varepsilon(E_1)}{\varepsilon(E_2)} \neq 1.$$

The relative efficiency ratio is:

$$\frac{\varepsilon(E_1)}{\varepsilon(E_2)} = \frac{R_1}{R_2},$$

and the corresponding fractional dropoff from E_1 to E_2 is:

$$\delta = 1 - \frac{\varepsilon(E_2)}{\varepsilon(E_1)} = 1 - \frac{R_2}{R_1}.$$

Uncertainties propagate, and for uncorrelated R_1, R_2:

$$\sigma_{\frac{R_1}{R_2}} = \frac{R_1}{R_2}\sqrt{\left(\frac{\sigma_{R_1}}{R_1}\right)^2 + \left(\frac{\sigma_{R_2}}{R_2}\right)^2}.$$

This class of SRD has a dropoff that can be modeled by a pwoer law [11]:

$$\varepsilon(E) = kE^{-n}.$$

$$n = \frac{\ln(\varepsilon(E_1)/\varepsilon(E_2))}{\ln(E_2/E_1)} = \frac{\ln(R_1/R_2)}{\ln(E_2/E_1)}.$$

Uncertainty in n becomes:

$$\sigma_n = \frac{\sigma_{R_1/R_2}}{(R_1/R_2)\,\ln(E_2/E_1)}.$$

For NaI(Tl) detectors, a $20-30\%$ dropoff in peak efficiency between 1.17 MeV and 1.33 MeV is typical for the commonly used crystals [11].

3 Data Analysis and Results

3.1 Fitting Energy Droppoff

Following the theory outlined in section 2.6, we can correct for detector dropoff before doing our statistical analysis. Using our Co-60 data and the energy calibration from calculations in section section 2.3, we extract measured rates (counts per second) and ratios for our runs. Table 1 displays this data.

The mean efficiency ratio is:

$$\frac{\varepsilon(1.17)}{\varepsilon(1.33)} = 1.3050 \pm 0.0011,$$

corresponding to a dropoff of:

$$\delta = 23.37\% \pm 0.06\%.$$

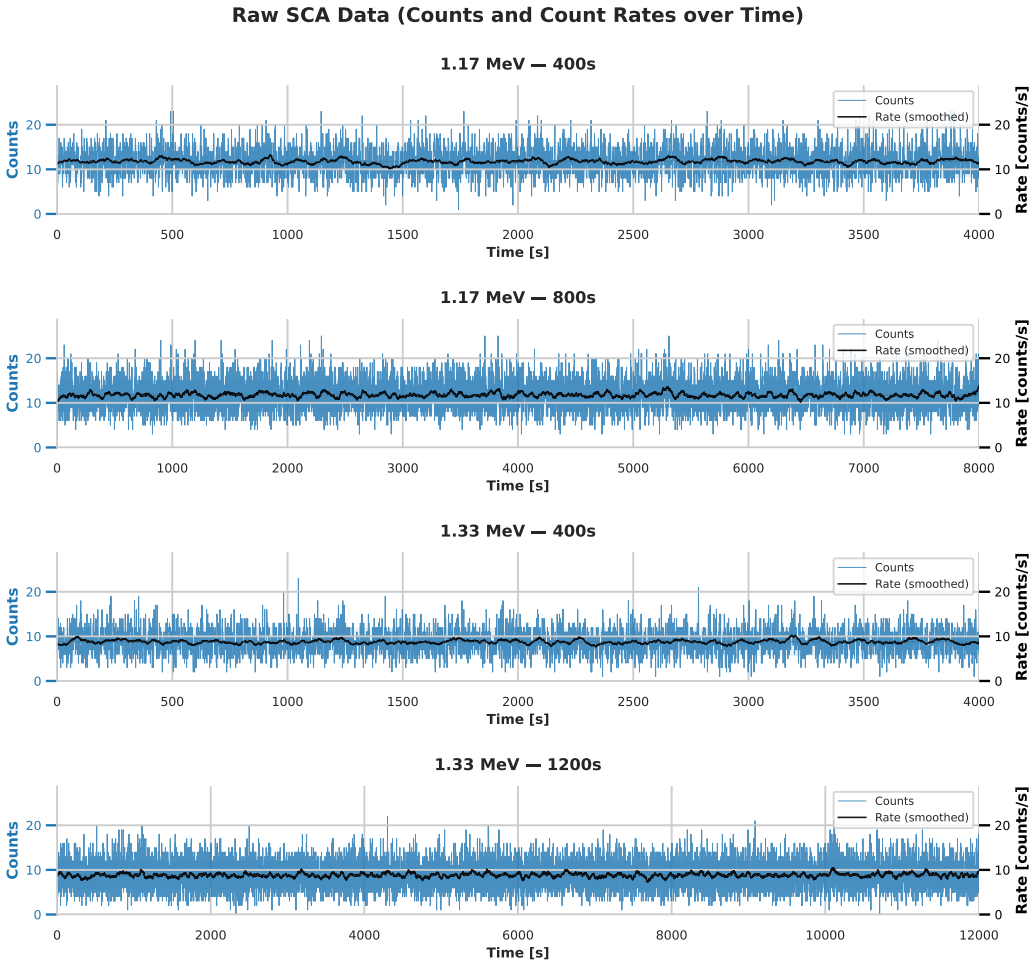

Figure 4: Raw SCA data measured at the two Co-60 peaks and with varying collection times. Both total recorded events as well as count rates are shown, and the data shows stochastic and random characteristics.

From the power-law relation, we find:

$$n = 2.091 \pm 0.007.$$

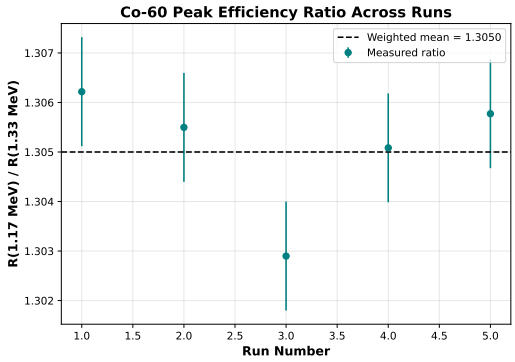

Figure 6: Measured efficiency ratio across runs, showing weighted mean compared to individual ratios. The consistent ratio validates the modeled energy-dependent dropoff.

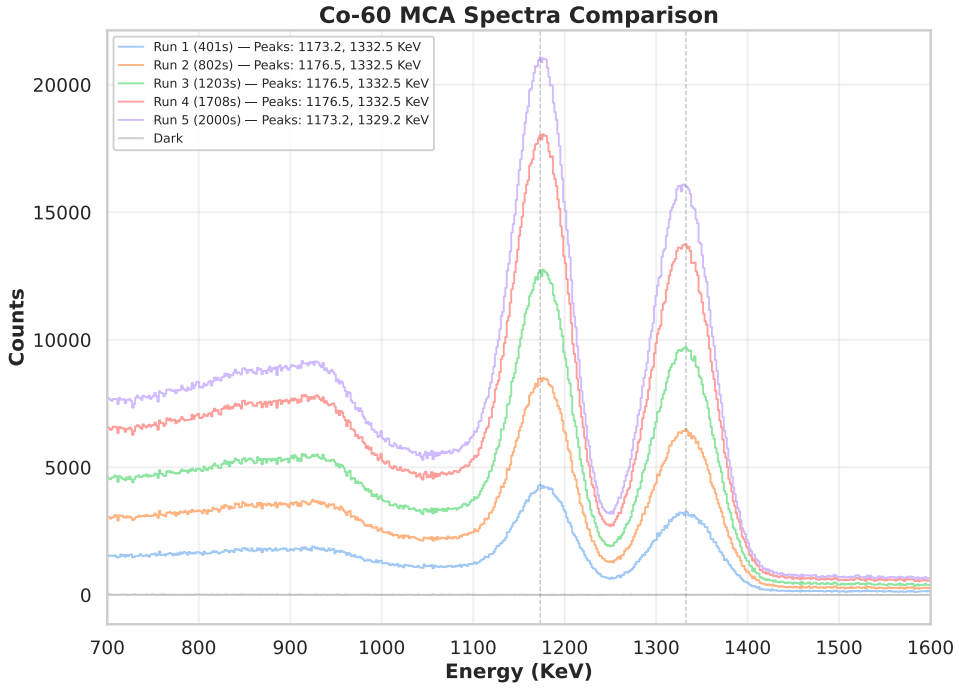

Figure 5: Five MCA measurements of the decaying Co-60 source taken with varying runtimes, with live runtime shown in the legend. This shows the characteristic spectra of the source, with two gamma ray peaks at the high-energy peart of the spectrum. The peak height can be visually seen to grow faster than the width.

Our measured efficiency ratio of 1.305 ± 0.001 shows that the detector is about 30.5% more efficient at detecting the 1.17 MeV photopeak than the 1.33 MeV one. This is a $\sim 23\%$ relative dropoff, which is quite close to the expected 25−30% efficiency decrease reported for NaI(Tl) detectors in the 1–2 MeV range [11]. This supports the validity of our measurements and analysis of the detector's properties.

3.2 Rates of Decay

To determine whether or not the rates of the decay process are equal, we can perform a paired t-test with the null hypothesis that:

$$H_0 : \ R_{1.17} = R_{1.33}, \qquad H_a : \ R_{1.17} \neq R_{1.33}.$$

As shown in section 2.6, NaI(Tl) detectors exhibit an efficiency dropoff with increasing energy, so we expect $R_{1.17} > R_{1.33}$. We can test whether the observed difference is actually statistically significant.

The sample mean and standard deviation are:

$$\bar{d} = 125.89, \qquad s_d = 0.59.$$

With $n = 5$ runs, we can calculate the the standard error:

$$s_{\bar{d}} = \frac{s_d}{\sqrt{n}} = \frac{0.59}{\sqrt{5}} = 0.26.$$

Then the test statistic is:

$$t = \frac{\bar{d} - 0}{s_{\bar{d}}} = \frac{125.89}{0.26} \approx 484.$$

With $\nu = 4$ degrees of freedom, the p-value is $p < 10^{-8}$.

Si we can very safely reject the null hypothesis that $R_{1.17} = R_{1.33}$.

$$\frac{R_{1.17}}{R_{1.33}} = 1.3050 \pm 0.0011,$$

or a $23.37\% \pm 0.06\%$ dropoff, which matches theoretical expectations for NaI(Tl) detectors [11].

The 95% confidence interval for $\bar{d}$ is given by

$$\bar{d} \pm t_{0.975,\nu}\, s_{\bar{d}}.$$

Using $t_{0.975,4} = 2.776$, we find:

$$125.89 \pm 2.776(0.26) \quad \Rightarrow \quad [125.17,\ 126.61].$$

Table 1: Measured Co-60 peak count rates and ratios.

Run	$R_{1.17}$ (cps)	$R_{1.33}$ (cps)	$R_{1.17}/R_{1.33}$
1	540.50	413.79	1.306
2	539.04	412.90	1.305
3	538.11	413.01	1.303
4	537.59	411.92	1.305
5	537.43	411.58	1.306
Weighted Mean	538.02 ± 0.30	412.27 ± 0.26	1.3050 ± 0.0011

Table 2: Measured count rates for each of the two primary γ peaks in the Co-60 source detected by the SRD across 5 different runs. We find that the ratio of the two count rates is significantly different from each other on each run, and on average.

Since the interval does not include 0, the difference is very significant.

Then, both of our tests confirm that the 1.17 MeV peak is measured at a significantly higher rate than the 1.33 MeV peak, which is completely consistent with our efficiency dropoff derived earlier.

3.3 Distribution Analysis

As discussed in section 1.2, when the mean count N becomes sufficiently large, the discrete Poisson distribution approaches a normal distribution.

The common rule is that the Poisson distribution can be approximated by a Gaussian when the number of events is around

$$N > 20$$

We analyzed the count distributions around the two primary peaks across multiple collection times. For each peak, we used a ± 50 channel region around the peak and compared Poisson and Gaussian fits using the Kolmogorov–Smirnov (D) statistic, reduced chi-squared (χ^2), and log-likelihood (LL) metrics which are discussed in section 1.2. Table 3 shows these results.

For all four cases, the mean count rate was approximately $\mu \approx 47$–48 counts per interval. The Gaussian fit had smaller KS statistics ($D_G < D_P$), lower χ^2 values, and significantly higher log-likelihoods, which means that the Gaussian model provides a better description of the true distribution when the mean is larg. Figures 7 and 8 show that the Gaussian curve follows the observed distribution, while the Poisson fit underestimates the width and tails.

For small mean values ($\mu < 20$), the Poisson nature of counting statistics is very clear to see. The probability becomes concentrated near low count values, which makes a right-skewed shape that is very unlike a Gaussian.

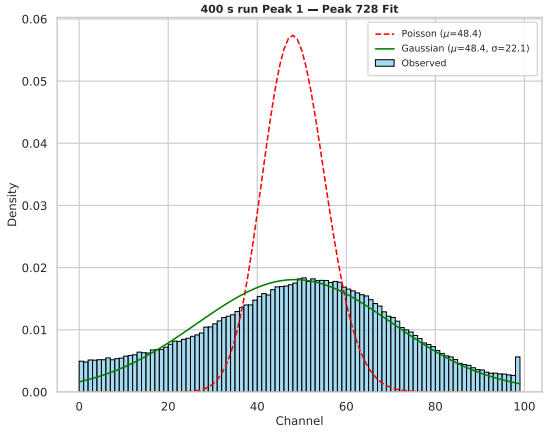

Figure 7: Distribution of counts for a 400 s run, Peak 1 ($\mu = 48.4$, $\sigma = 22.1$). The Gaussian fit matches the observed spread, while the Poisson model is too narrow.

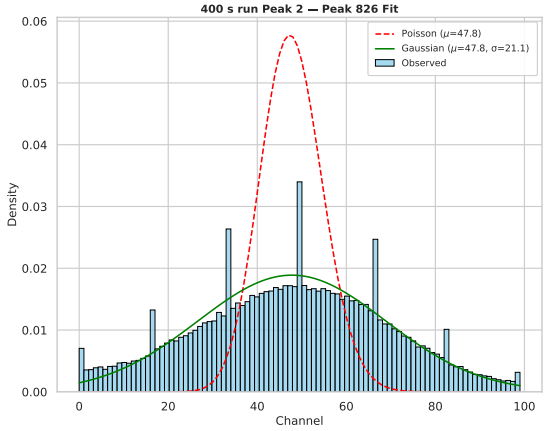

Figure 8: Distribution of counts for the 400 s run, Peak 2 ($\mu = 47.8$, $\sigma = 21.1$). The Gaussian fit again provides a better representation of the data.

To visualize how fit quality evolves over time, Figures 9

Table 3: Quantitative Fit Comparison Between Poisson and Gaussian Models

Run	Peak	μ	σ	D_{P}	D_{G}	χ^2_{P}	χ^2_{G}
400 s	1 (728)	48.44	22.08	0.278	0.028	0.0139	0.0003
400 s	2 (826)	47.77	21.12	0.270	0.020	0.0135	0.0004
800 s	1 (730)	46.99	21.94	0.274	0.023	0.0139	0.0002
800 s	2 (826)	47.56	21.09	0.270	0.020	0.0133	0.0001

Table 4: Different statistical analysis scores for Poisson and Gaussian distribution. The KS statistics show that the Poisson distribution had a much worse fit to the data than the Gaussian distribution in the limit of $N >> 20$, and the very low χ^2 values for the Gaussian fit indicate that the Gaussian model is a stronger model for this system.

and 10 plot the KS statistics for both models alongside mean count rate. The Gaussian D statistic remains consistently lower across all samples, further demonstrating superior performance in the high-count regime.

We can also calculate standard deviations for this distribution across multiple runs with low N, i.e when a Poissonian distribution would be a better model than a normal distribution. In this regime, we find that the standard deviation for the $1.17MeV$ peak (averaged across 3 runs) for $N = 15$ is $\sigma = 6.89$, which is approximately $\sqrt{\mu}$ where the means are shown in table 3. We neglect any errors here because of the discrete nature of the counts and extremely small time scales of the runs we use, which wouuld result in negligible errors.

3.4 Allan Variance

Corresponding to the outlined theory in 1.2, we computed the Allan deviation for the two SCA energy channels centered at 1.17 MeV and 1.33 MeV over a 400 s acquisition. The resulting Allan deviation curves are shown in Figure 11.

At short averaging times ($\tau < 50$ s), both runs have slope that matches $\tau^{-1/2}$, confirming that the fluctuations are due to Poisson counting noise. The 1.33 MeV channel shows a slightly lower deviation, consistent with its higher mean count rate. For $\tau > 100$ s, both curves begin to deviate from the ideal slope. This could be due to correlated drift or slow systematic variations in the detection electronics or source emission.

3.5 Interrarival Time Analysis

Since our SCA data records binned counts at 1 s intervals, we approximated individual event times by uniformly distributing the recorded counts within each bin. We then computed the interarrival times outline in section 1.3.

Figure 12 shows the interarrival time distribution for the 1.33 MeV channel. The measured histogram (blue) aligns closely with the expected exponential decay (black dashed line), with a fitted mean rate of $\lambda = 7.85\,\mathrm{s}^{-1}$. This confirms that the detection process is consistent with an uncorrelated, memoryless distribution, which is expected for a Poisson.

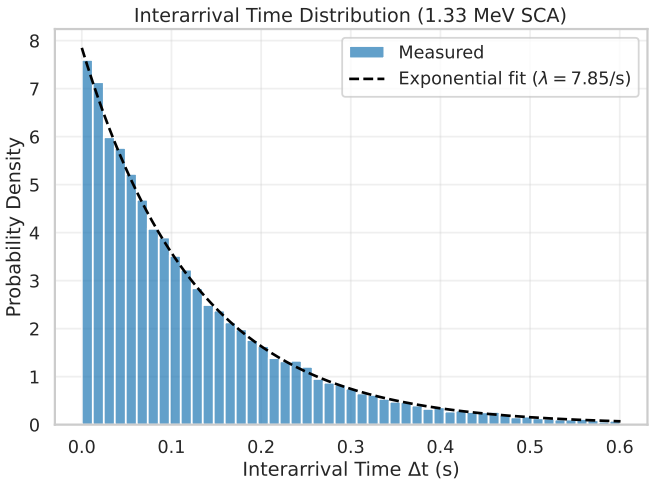

Figure 12: Interarrival time distribution for the 1.33 MeV SCA channel. The blue histogram represents measured intervals reconstructed from binned counts, while the dashed curve shows the exponential PDF $p(\Delta t) = \lambda e^{-\lambda \Delta t}$ fitted with $\lambda = 7.85\,\mathrm{s}^{-1}$.

4 Conclusion and Discussion

4.1 Results and Brief Discussion

Our analysis confirms our expectations: as μ increases, the Poisson distribution becomes Gaussian, and for $\mu \approx 50$ the Gaussian fit outperforms Poissonian fits. For large mean counts ($\mu > 20$), the Poisson distribution is well-approximated by a Gaussian, as verified by KS and χ^2 tests. For small mean counts ($\mu < 10$), the distribution

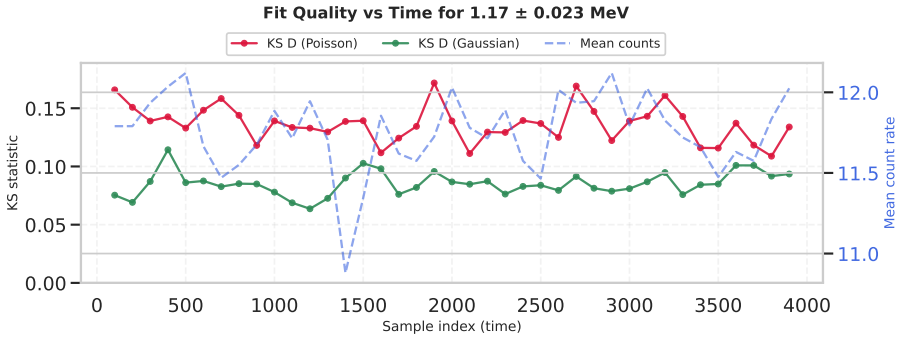

Figure 9: Fit quality versus time for the 1.17 MeV peak. The Gaussian model (green) consistently yields smaller KS D values than the Poisson (red), confirming better agreement for large μ.

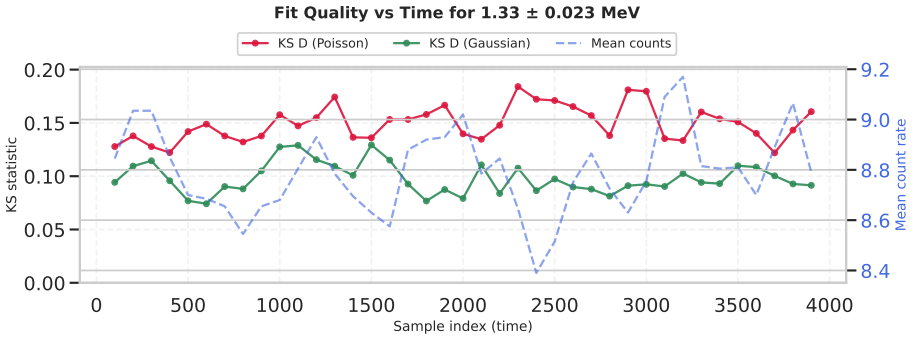

Figure 10: Fit quality versus time for the 1.33 MeV peak. Similar behavior is observed, with the Gaussian fit outperforming the Poisson model across all intervals with large N.

remains right-skewed and distinctly Poissonian. The decay rates of the two processes differ significantly, with $R_{1.17}/R_{1.33} = 1.3050 \pm 0.0011$ ($p < 10^{-8}$), consistent with NaI(Tl) efficiency dropoff. The measured standard deviation follows $\sigma_N = \sqrt{N}$, confirming the expected Poisson scaling. We went beyond distributional analysis and examined time-domain properties of the detection process using interarrival time and Allan variance analyses. The interarrival time analysis constructed distribution closely followed the exponential probability density $p(\Delta t) = \lambda e^{-\lambda \Delta t}$ with a fitted rate of $\lambda = 7.85\,\mathrm{s}^{-1}$, confirming that detections occur randomly and independently, as expected for a memoryless Poisson process. The Allan variance of the count-rate time series for both the 1.17 MeV and 1.33 MeV channels. The Allan deviation $\sigma_y(\tau)$ exhibited a slope of $\tau^{-1/2}$ at short averaging times, consistent with uncorrelated white noise behavior, and flattened at longer τ, indicating the presence of slow drift or correlated fluctuations in the system. Both energy channels showed similar scaling and crossover points, suggesting they share the same underlying noise processes. Together, these results confirm that our data exhibits a Poisson distribution when measured on short timescales.

4.2 Conclusion

The goals of this experiment were to measure and characterize the decay processes of Co-60, including rigorous statistical analysis. To accomplish this, we utilized scintillation radiation detectors and signal processing equipment that allowed use to determine that a statistically significant difference of 1.3050 ± 0.0011 exists in the rates of decay of the two processes, the standard deviation of the distribution exhibited Gaussian behavior for large N, and Poisson behavior for small N. Finally, we carried out temporal analysis to find a $p = 0.52$ exponential waiting time probability as well as an Allan variance exponen-

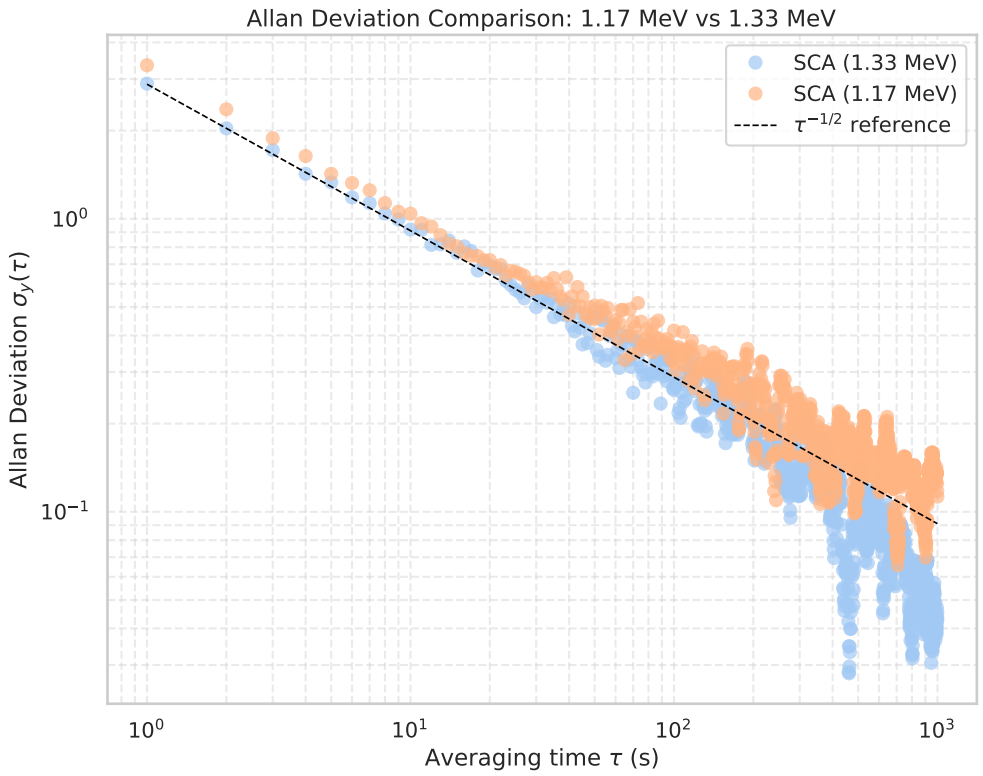

Figure 11: Allan deviation $\sigma_y(\tau)$ as a function of averaging time τ for the 1.17 MeV and 1.33 MeV SCA channels. The dashed line represents the theoretical $\tau^{-1/2}$ dependence expected for Poisson noise. Deviations at large τ indicate correlated noise or drift.

tial fit to characterize noise variance across time and find $\tau^{-1/2}$ relations that are expected for Poisson noise. These results demonstrate the underlying statistical nature of decay, and this experiment has been a valuable exercise in data collection, statistical analysis, and independent laboratory procedure.

4.3 Future Work Considerations

Future work might consider utilizing an SRD that has correction for high energy photon dropoff responses, or a known calibration to recover the actual counts as a function of energy, to avoid having to quantify the detector response as we did. Additionally, multiple functioning PMTs and SRDs would be very beneficial as systematic errors could be reduced by relying on multiple instrument readings. We regret that our second SRD was not able to be used due to a lack of functioning signal processing equipment to use it. Another potential improvement is to use SCAs that have kown energy to dial translations, so that doing a linear fit to determine these parameters (which could introduce error) is not necessary. Finally, future experiments could utilize different atoms and compare their statistics to those of Co-60.

References

[1] D. W. Allan. "Statistics of Atomic Frequency Standards". In: *Proceedings of the IEEE* 54.2 (1966), pp. 221–230. DOI: 10.1109/PROC.1966.4634.

[2] et al. Cui. "The Kolmogorov-Smirnov Statistic Revisited". In: (). URL: https://arxiv.org/abs/2503.11673.

[3] IAEA. "Investigation of Uncertainty Sources in the Determination of Gamma Emitting Radionuclides in the UAL". In: (). URL: https://www-ns.iaea.org/downloads/rw/ppss/quality-management/uncertainty-gamma-measurement.pdf?utm_source=chatgpt.com.

[4] Glenn F. Knoll. *Radiation Detection and Measurement*. 2nd ed. New York: John Wiley & Sons, 1989.

[5] Openstax. *Discovery of Radioactivity*. Chemistry LibreTexts. URL: https://chem.libretexts.org/Bookshelves/Physical_and_Theoretical_Chemistry_Textbook_Maps/Supplemental_Modules_(Physical_and_Theoretical_Chemistry)/Nuclear_Chemistry/Radioactivity/Discovery_of_Radioactivity.

[6] Openstax. *Nuclear Decay and Conservation Laws*. Chap. 31.4. URL: https://openstax.org/books/college-physics-2e/pages/31-4-nuclear-decay-and-conservation-laws.

[7] Openstax. *Poisson Distribution*. Statistics LibreTexts. URL: https://stats.libretexts.org/Bookshelves/Introductory_Statistics/Mostly_Harmless_Statistics_(Webb)/05%3A_Discrete_Probability_Distributions/5.06%3A_Poisson_Distribution.

[8] Openstax. *Radioactive Decay*. Physics LibreTexts. URL: https://phys.libretexts.org/Bookshelves/University_Physics/University_Physics_(OpenStax)/University_Physics_III_-_Optics_and_Modern_Physics_(OpenStax)/10%3A__Nuclear_Physics/10.04%3A_Radioactive_Decay.

[9] Openstax. *Renewal Processes: Introduction*. Statistics LibreTexts. URL: https://stats.libretexts.org/Bookshelves/Probability_Theory/Probability_Mathematical_Statistics_and_Stochastic_Processes_(Siegrist)/15%3A_Renewal_Processes/15.01%3A_Introduction.

[10] Ortec. "905 Series NaI(Tl) Scintillation Radiation Detectors". In: (). URL: https://www.ortec-online.com/products/radiation-detectors/scintillation-radiation-detectors/scintillation-detector-types/905-series.

[11] Ortec. "Gamma-Ray Spectroscopy Using NaI(Tl)". In: (). URL: https://www.ortec-online.com/-/media/ametekortec/third%20edition%20experiments/3-gamma-ray-spectroscopy-using-nai-tl.pdf?utm_source=chatgpt.com.

[12] Ortec. "Simply Managing Dead Time Errors in Gamma-Ray Spectrometry". In: (). URL: https://www.ortec-online.com/-/media/ametekortec/application%20notes/an63.pdf?la=en&.

[13] Enrico Rubiola. "On the measurement of frequency and of its sample variance with high-resolution counters". In: (). URL: https://web.archive.org/web/20110720220221/http://www.femto-st.fr/~rubiola/pdf-articles/journal/2005rsi-hi-res-freq-counters.pdf.